# Influence of Chromium Alloying on the Cyclic Oxidation Behavior of Nanocrystalline $(Mo_xCr_{1-x})_5Si_3$ Films at 800 °C in Air

Jiang Xu,*,[†] Shuyun Jiang,[‡] and Yue Wang[†]

Department of Material Science and Engineering, Nanjing University of Aeronautics and Astronautics, 29 Yudao Street, Nanjing 210016, People's Republic of China, and Department of Mechanical Engineering, Southeast University, 2 Si Pai Lou, Nanjing 210096, People's Republic of China

**ABSTRACT** In order to investigate the influence of the chromium content on the oxidation performance of the chromium-alloyed $Mo_5Si_3$, five kinds of sputter-deposited nanocrystalline $(Mo_xCr_{1-x})_5Si_3$ ($x = 1, 0.78, 0.75, 0.64, 0.57$) films have been prepared on Ti−6A1−4 V alloy substrates by double-cathode glow discharge. X-ray diffraction, scanning electron microscopy, and transmission electron microscopy have been used to characterize the nanocrystalline $(Mo_xCr_{1-x})_5Si_3$ ($x = 1, 0.78, 0.75, 0.64, 0.57$) films. The as-deposited films were free of crack having metallurgical bonding with a substrate and consisted of an outer $(Mo_xCr_{1-x})_5Si_3$ layer and an inner diffusion layer. The inner diffusion layer could be divided into a $\beta$-phase layer with high Mo content (>10 wt %) and an $\alpha''/\alpha'$ layer with low Mo content (<10 wt %). During the cyclic oxidation test at 800 °C in air, for the monolithic nanocrystalline $Mo_5Si_3$ film, local spallation of the oxide scale took place by internal stresses after 5 min of oxidation, and severe spallation of the oxide scale sharpened the mass loss with an increase in the oxidation time. However, in the case of nanocrystalline chromium-alloyed $Mo_5Si_3$ films, spallation resistance to thermal cycling increased significantly with an increase in the chromium addition, and particularly for the $(Mo_{0.57}Cr_{0.43})_5Si_3$ film, no sign of spallation or microcracking occurred even after 240 h at 800 °C because of the formation of a fine-grain protective scale.

**KEYWORDS:** molybdenum silicides • nanostructured intermetallics • alloy design • cyclic oxidation • double-cathode glow discharge

## INTRODUCTION

Refractory metal silicides are of interest as high-temperature structural materials because of their ultrahigh melting temperatures, chemical stability at elevated temperatures, and elevated temperature strength (1−3). Compared with other refractory metals, molybdenum silicide based intermetallic compounds are attractive material systems because Mo has a lower density (4). Among the compounds of molybdenum silicides, D8m-structured $Mo_5Si_3$ is the most refractory compound, having a melting point of 2180 °C, and shows lower creep rates than $MoSi_2$ at high temperatures, thus having a great potential for structural applications in harsh environments (5−7). Unfortunately, there are still some drawbacks that have hindered its use as a structural material. First, similar to most high-temperature intermetallics, the $Mo_5Si_3$ intermetallic compound is intrinsically brittle at ambient temperatures (8). Second, owing to noncubic tetragonal crystal structures, its coefficient of thermal expansion (CTE) is highly anisotropic (9). Third, it suffers from catastrophic oxidation at 800 °C, showing low-temperature "pest" (disintegration into a pow-

der) behavior similar to that commonly observed in the low-temperature oxidation of $MoSi_2$ (10).

The oxidation behavior of molybdenum silicide alloys is predominantly governed by exposure conditions, which determine the relative growth rates of silica and molybdenum oxide. In the pest temperature regime, molybdenum silicide alloys oxidize to form $MoO_3$ and $SiO_2$, and volatilization of $MoO_3$ leaves a porous silica layer behind (11). However, the limited silica growth rate makes it impossible to seal pores that initially form in the scale (12). The porous and poorly protective silica facilitates the fast oxygen transport to the oxide/molybdenum silicide interface, causing a wedging effect from the oxide growth in these defects. This results in an increased oxidation rate and a subsequent accelerated oxidation and/or pesting behavior (13). During recent decades, three important routes currently being pursued to control the pest oxidation of molybdenum silicide alloys are substitutional alloying (14−16), the addition of a ceramics phase (17), and high-temperature preoxidation treatment (18). Alloying approaches to improve the oxidation resistance of molybdenum silicide alloys are, however, much more promising. As the main alloying elements, additions of chromium to molybdenum silicides have been observed to give the best results because a stable oxide is formed that would prevent the formation of highly volatile molybdenum oxides. For example, Ochiai (19, 20) studied the oxidation-proof property of a $Mo_3Si$ intermetallic alloy through the addition of chromium and aluminum elements.

He reported that the essentially effective agent for the improvement of the oxidation in $Mo_5Si$ is chromium and the effect of aluminum is secondary to the effect of chromium.

To the best of our knowledge, there were no reports available in the literature with regard to the oxidation performance of chromium-alloying nanocrystalline $(Mo_xCr_{1-x})_5Si_3$ either as bulk or coating materials. In our previous work (21, 22), we have found that the double-cathode glow discharge technique can be used to synthesize a nanocrystalline $Al_2Mg$ film and a nanocrystalline $Cr_3Si$ film with a grain size of <5 nm on magnesium and titanium alloys, respectively. In this paper, the $(Mo_xCr_{1-x})_5Si_3$ ($x = 1$, 0.78, 0.75, 0.64, 0.57) films with an average grain size of about 8 nm were deposited onto Ti−6A1−4 V alloy substrates by glow discharge. The main purpose of the present work is to explore a coupling effect of the nanosize crystal and substitution of chromium for molybdenum on the oxidation performance of a nanocrystalline $Mo_5Si_3$ film.

## MATERIALS AND METHODS

**Preparation Processes of Films.** The nanocrystalline $(Mo_xCr_{1-x})_5Si_3$ films were deposited onto Ti−6A1−4 V alloy substrates by a double-cathode glow discharge apparatus, which was described in our previous papers (22). In the process of double-cathode glow discharge, one cathode is fabricated as the source (target) by desired sputtering materials, and the other cathode is substrate materials. When two different voltages are applied to the two cathodes, glow discharge comes into being. The glow discharge sputtering conditions are as follows: base pressure, $4 \times 10^{-4}$ Pa; target electrode bias voltage, −900 V; substrate bias voltage, −350 V; substrate temperature, 900 °C; working pressure, 35 Pa; parallel distance between the source electrode and the substrate, 15 mm; treatment time, 5 h. The sputter targets were fabricated by employing cold-compacting technology under a pressure of 600 MPa from ball-milled molybdenum (99.99 % purity), chromium (99.99 % purity), and silicon powders (99.99 % purity). The substrates were Ti−6Al−4 V alloy disks of 40 mm diameter and 3 mm thickness. The substrates were mechanically ground and progressively polished with a diamond paste. The polished substrates were then washed in acetone and ethanol by an ultrasonic washer. Five kinds of $(Mo_xCr_{1-x})_5Si_3$ ($x = 1$, 0.78, 0.75, 0.64, 0.57) films were deposited onto the substrate material by double-cathode glow discharge using five targets with different stoichiometric ratios ($Mo_{50}Si_{50}$, $Mo_{40}Cr_{10}Si_{50}$, $Mo_{35}Cr_{15}Si_{50}$, $Mo_{30}Cr_{20}Si_{50}$, and $Mo_{25}Cr_{25}Si_{50}$, respectively).

**Microstructure Characterization.** The phase composition of the as-deposited films was characterized with X-ray diffractometry (D8ADVANCE) operated at 35 kV and 40 mA. X-ray data were collected using a 0.1° step scan with a count time of 1 s. The etching of the $(Mo_xCr_{1-x})_5Si_3$ films was accomplished with the use of Kroll's reagent (10 mL of $HNO_3$, 4 mL of HF, and 86 mL of distilled water) for 20−30 s. The cross-sectional morphology and chemical composition of the as-deposited films were studied by scanning electron microscopy (SEM; Quanta200, FEI Company) and energy-dispersive X-ray spectroscopy (EDX), respectively. Transmission electron microscopy (TEM) and high-resolution TEM (HRTEM) images were observed by a JEOL JEM-2010 at an accelerating voltage of 200 kV. Thin foil samples for TEM observation were cut from an as-deposited film and were prepared by single-jet electropolishing from the untreated side of the substrate. Atomic force microscopy (AFM; Veeco Nanoscope V) was used to characterize the surface topographical characterizations and to measure roughness values for nanocrystalline $(Mo_xCr_{1-x})_5Si_3$ films. An area of 5 $\mu$m $\times$ 5 $\mu$m was
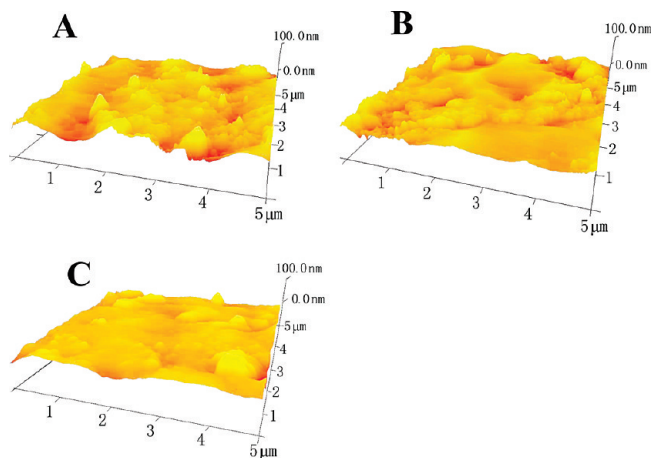


**FIGURE 1.** AFM 3D image of nanocrystalline $(Mo_xCr_{1-x})_5Si_3$ films deposited on Ti−6A1−4 V alloy substrates: (A) $Mo_5Si_3$ film; (B) $(Mo_{0.75}Cr_{0.25})_5Si_3$ film; (C) $(Mo_{0.57}Cr_{0.43})_5Si_3$ film.

measured under contact mode with tip NSC36 and a scan rate of 1.0 Hz for each measurement. Five areas of each sample with a minimum interval distance of 3 mm were measured to evaluate Rq (root-mean-square roughness average).

**Cyclic Oxidation.** Cyclic oxidation testing was performed in a box furnace at 800 °C in air. The temperature accuracy in the hot zone of the furnace was controlled within ±1 °C. The cyclic period was 5 h of heating in the furnace and 20 min of cooling outside the furnace. The mass changes of the specimens were measured on an analysis balance with an accuracy of 0.01 mg after every cycle. Afterward, the specimens were reintroduced into the furnace in order to continue the oxidation process. To exclude the exposed substrate material contribution to mass changes, the cyclic oxidation number for every specimen was determined by whether spallation of oxide scales occurred. As an exception, specimens of the $Mo_5Si_3$ film were given a total exposure of 10 min (four cycles) because of complete spallation of the film. After cyclic oxidation, the scale surfaces and/or cross sections of the specimens were examined with a scanning electron microscope equipped with an EDX analyzer and X-ray diffraction (XRD).

## RESULTS

**Microstructures of Nanocrystalline Films.** Figure 1 gives three-dimensional (3D) AFM images of three kinds of as-deposited nanocrystalline $(Mo_xCr_{1-x})_5Si_3$ ($x = 1$, 0.75, 0.57) films. The topographies of nanocrystalline $(Mo_xCr_{1-x})_5Si_3$ films exhibit a mountlike morphology and are rather smooth, with an average root-mean-square (Rq) roughness of 12.3 nm. Rahman et al. (23) reported that the roughness of magnetron-sputtered Ni−Al coatings was found to be 16.09 and 15.19 nm at substrate temperatures 300 and 350 °C, respectively. Çelik et al. (24) have also observed that the surface roughness of a forged CoCrMo alloy after plasma nitriding at 700 °C was measured between 0.23 and 0.45 $\mu$m, and the surface roughness increased with an increase in the treatment time and temperature. Thus, the surface morphologies of nanocrystalline $(Mo_xCr_{1-x})_5Si_3$ films were smoother than those obtained by other authors using different deposition methods. The smooth surface of the $(Mo_xCr_{1-x})_5Si_3$ films is considered to be beneficial to the formation of adherent and protective oxide scales when they are exposed to high-temperature environments.
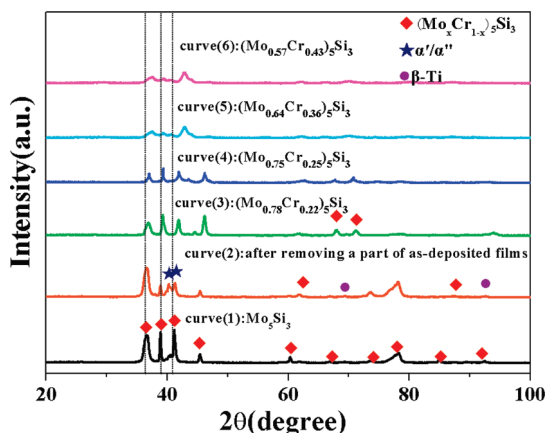
FIGURE 2. XRD pattern of the sputter-deposited $(Mo_xCr_{1-x})_5Si_3$ films.

The XRD patterns of the five kinds of sputter-deposited $(Mo_xCr_{1-x})_5Si_3$ ($x = 1$, 0.78, 0.75, 0.64, 0.57) films are presented in Figure 2. The XRD patterns are characterized by a set of broad peaks indexed as a D8m-structured $Mo_5Si_3$ phase (JCPDS Card No. 76-1578), indicating that all of the sputter-deposited films consist of a single phase of $(Mo_xCr_{1-x})_5Si_3$, and the phase composition of the as-deposited films is independent of the substitution of chromium for molybdenum. This is due to the fact that $Cr_5Si_3$–$Mo_5Si_3$ is an infinitive solid-solute system and the chemical bond of the Cr atom in the D8m system is considered to be similar to that of Mo atoms. Thereby, the formation of second phases never occurs with the substitution of chromium for the molybdenum site in $Mo_5Si_3$. Furthermore, owing to the fact that the Cr atom is smaller than the Mo atom, the diffraction peaks gradually shift to higher $2\theta$ compared with the powder diffraction file data for $Mo_5Si_3$ with decreasing $x$, indicating a lattice contraction. This is in accordance with the results reported in ref 25. Parts A and B of Figure 3 show SEM cross-sectional morphology of the sputter-deposited $Mo_5Si_3$ film and the $(Mo_{0.75}Cr_{0.25})_5Si_3$ film formed on a Ti–6Al–4 V alloy, respectively. Clearly, the films are devoid of pores and microcracks and appear compact and quite well-adhered to the Ti–6Al–4 V alloy substrate. The microstructures of two kinds of $(Mo_xCr_{1-x})_5Si_3$ ($x = 1$, 0.75) films can be classified into two uniform layers, namely, a deposited layer and a diffusion layer. The deposited layer contains mostly Mo (or Mo + Cr) and Si, and the Mo (or Mo + Cr) and Si concentrations across the depth of the deposited layer remain almost constant with a molar ratio of Mo (or Mo+Cr) to Si close to 1.66, indicating that the deposited layer is composed of a single $(Mo,Cr)_5Si_3$ phase. In order to understand the constituent phases of the diffusion layer, the phases present in the diffusion layer were identified by XRD after removal of a part of the $Mo_5Si_3$ deposited layer, and its XRD pattern is plotted in Figure 2 (curve 2). A comparison between curves 1 and 2 (Figure 2) shows that the diffusion layer is a composite of $\beta$-Ti, $\alpha''$, and $\alpha'$ phases. Because the dominant diffusion element in the $Mo_5Si_3$ phase is molybdenum (26), the Mo element diffuses inward into the interface between the deposited layer and the substrate, leading to the phase transformation of $\beta \rightarrow \alpha'' \rightarrow \alpha'$, which occurs
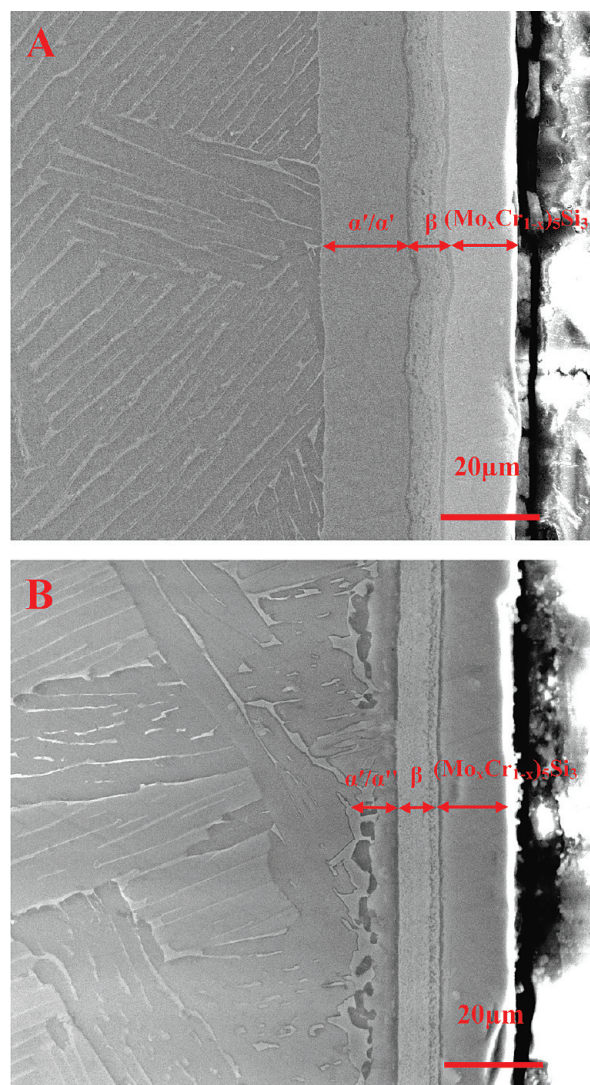


FIGURE 3. SEM observation of the sputter-deposited $(Mo_xCr_{1-x})_5Si_3$ films formed on a Ti–6Al–4 V alloy: (A) $Mo_5Si_3$ film; (B) $(Mo_{0.75}Cr_{0.25})_5Si_3$ film.

from outside to inside for the different molybdenum contents in the diffusion layer (27). When the XRD results and EDS analysis are combined, conclusions can be made that, according to the different molybdenum contents, the molybdenum diffusion layer may be subdivided into a $\beta$-phase layer with high molybdenum content (>10 wt %) and an $\alpha''/\alpha'$ layer with low molybdenum content (10 wt %), as shown in Figure 3. Beyond this, it is worthwhile noting that the thickness of the diffusion layer is affected by its chromium content, and the higher chromium content in the diffusion layer results in a thinner thickness, implying that chromium restricts molybdenum migration from the deposited layer to the substrate. The gradient distribution of alloying elements in the diffusion layer offers a smooth transition of the thermal expansion coefficient, which is conducive to reducing the thermal stresses induced by the mismatch of thermal expansion coefficients between the deposited layer and the substrate during cyclic oxidation testing.

Figure 4 shows the typical HRTEM image and selected-area electron diffraction (SAED) patterns of the $Mo_5Si_3$ film. The microstructure is composed of randomly oriented spheri-
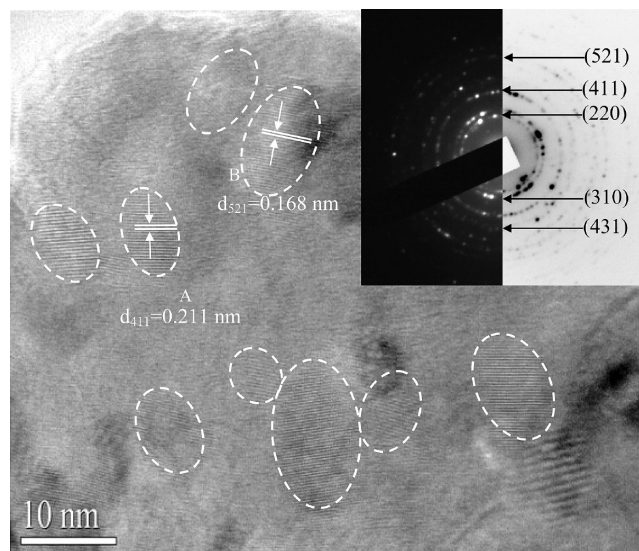
**FIGURE 4.** HRTEM images and the corresponding SAED pattern of the nanocrystalline $Mo_5Si_3$ film. Some of the nanocrystallites are circled for easier recognition. The space of the lattice fringes of nanocrystalline films marked as A and B can be calculated as 0.211 and 0.168 nm, which correspond to the interspacing of the (411) and (521) planes of D8m-structured $Mo_5Si_3$, respectively.
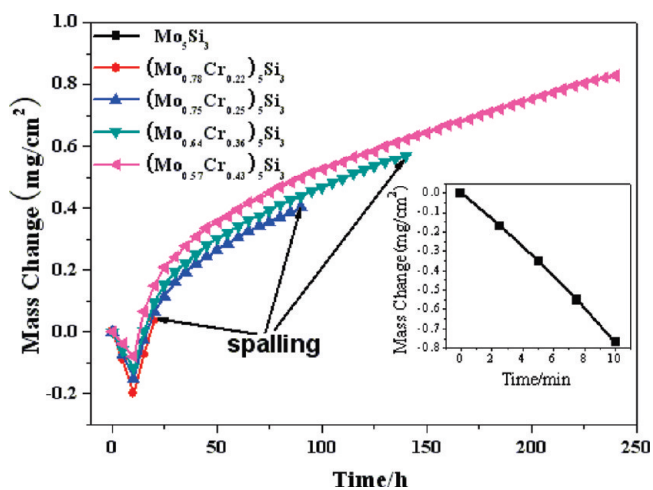


**FIGURE 5.** Mass change as a function of the exposure time for the sputter-deposited $(Mo_xCr_{1-x})_5Si_3$ films at 800 °C in air.

cal crystallites with an average grain size of ∼8 nm. The space of the lattice fringes of nanocrystalline films marked as A and B can be calculated as 0.211 and 0.168 nm, which correspond to the interspacing of the (411) and (521) planes of D8m-structured $Mo_5Si_3$, respectively. The diffraction rings of SAED (inset in Figure 4) correspond to the (220), (310), (411), (431), and (521) planes of the D8m crystal structure $Mo_5Si_3$, respectively.

**Cyclic Oxidation Kinetics.** Figure 5 shows the cyclic oxidation kinetic curves of the sputter-deposited nanocrystalline $(Mo_xCr_{1-x})_5Si_3$ films at 800 °C in air. The average rate constants for the oxidation of nanocrystalline $(Mo_xCr_{1-x})_5Si_3$ films at 800 °C are summarized in Table 1. It can be seen that two main trends in the kinetic character are observed for different $(Mo_xCr_{1-x})_5Si_3$ films. The kinetic curve of the $Mo_5Si_3$ film exhibits an almost linear weight loss rate ($-4.63$ mg cm$^{-2}$ h$^{-1}$), the value of which is close to the result

## Table 1. Rate Constants for the Oxidation of Nanocrystalline $(Mo_xCr_{1-x})_5Si_3$ Films

| specimen | kinetic model | steady-state rate constant[a] | run time |
|---|---|---|---|
| $Mo_5Si_3$ | linear | $-4.63$ | 10 min |
| $(Mo_{0.78}Cr_{0.22})_5Si_3$ | linear | $2.33 \times 10^{-2}$ | 10−20 h |
| $(Mo_{0.75}Cr_{0.25})_5Si_3$ | parabolic | $2.26 \times 10^{-3}$ | 10−90 h |
| $(Mo_{0.64}Cr_{0.36})_5Si_3$ | parabolic | $2.62 \times 10^{-3}$ | 10−140 h |
| $(Mo_{0.57}Cr_{0.43})_5Si_3$ | parabolic | $2.96 \times 10^{-3}$ | 10−240 h |

[a] Rate constants are given in units of mg cm$^{-2}$ h$^{-1}$ for linear rates and mg$^2$cm$^{-4}$ h$^{-1}$ for parabolic rates. A negative rate indicates mass loss.

## Table 2. Phases Identified in the XRD Patterns of the Oxide Scales Formed on the Nanocrystalline $(Mo_xCr_{1-x})_5Si_3$ Films after Different Times of Oxidation at 800 °C in Air

| specimen | total oxidation time | oxidation products |
|---|---|---|
| $Mo_5Si_3$ | 5 min | $MoO_3$, $SiO_2$ |
| | 10 min | $TiO_2$, $SiO_2$ |
| $(Mo_{0.78}Cr_{0.22})_5Si_3$ | 20 h | $Cr_2O_3$, $SiO_2$, $Cr_2(MoO_4)_3$ |
| $(Mo_{0.75}Cr_{0.25})_5Si_3$ | 90 h | $Cr_2O_3$, $SiO_2$, $Cr_2(MoO_4)_3$ |
| $(Mo_{0.64}Cr_{0.36})_5Si_3$ | 140 h | $Cr_2O_3$, $SiO_2$, $Cr_2(MoO_4)_3$ |
| $(Mo_{0.57}Cr_{0.43})_5Si_3$ | 240 h | $Cr_2O_3$, $SiO_2$, $Cr_2(MoO_4)_3$ |

obtained by Natesan and Deevi (12), who have reported that the $Mo_5Si_3$ alloy produced by hot-pressing exhibited an almost linear weight loss rate ($-6.6$ mg cm$^{-2}$ h$^{-1}$) during the oxidation test at 800 °C. For chromium-alloying nanocrystalline $(Mo_xCr_{1-x})_5Si_3$ ($x = 0.78, 0.75, 0.64, 0.57$) films, the kinetic curves are, in general, characterized by the rapid weight loss during an initial period of 10 h and the subsequent steady-state oxidation with weight gain that are found to follow a parabolic relationship, except that nanocrystalline $(Mo_{0.78}Cr_{0.22})_5Si_3$ films have a rapid linear mass gain. The extent of the rapid mass loss at the initial oxidation of 10 h decreases with an increase in the chromium content in the films. Furthermore, spallation resistance to thermal cycling for nanocrystalline $(Mo_xCr_{1-x})_5Si_3$ films is strongly dependent on the chromium content, and the higher the chromium content, the higher the spallation resistance. The experimental observations show that, in the case of nanocrystalline $(Mo_xCr_{1-x})_5Si_3$ ($x = 0.78, 0.75, 0.64$) films, oxide-scale spallation occurred after exposure of 20, 90, and 140 h at 800 °C in air, respectively. Nevertheless, for a nanocrystalline $(Mo_{0.57}Cr_{0.43})_5Si_3$ film, no sign of spallation or microcracking occurs even after 240 h at 800 °C.

**Oxidation Products.** The constituents of the oxide scales formed on the nanocrystalline $(Mo_xCr_{1-x})_5Si_3$ films exposed at 800 °C for different times identified by XRD are summarized in Table 2. Figure 6 shows the typical XRD patterns taken from the surfaces of the $Mo_5Si_3$ film after oxidation tests for 5 and 10 min at 800 °C in air. After 5 min of exposure at 800 °C in air, XRD analyses have only shown the peaks of $MoO_3$, whereas after 10 min of exposure, only X-ray peaks for $TiO_2$ are detected, confirming that the exposed interior Ti−6A1−4 V alloy substrate is oxidized because of severe spallation of the film. Figure 7 shows the XRD patterns of nanocrystalline $(Mo_{0.57}Cr_{0.43})_5Si_3$ films after
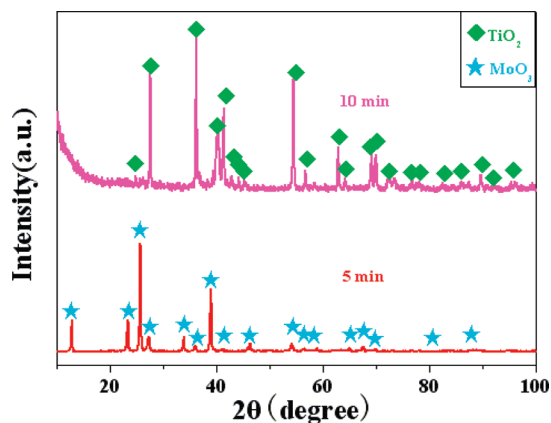
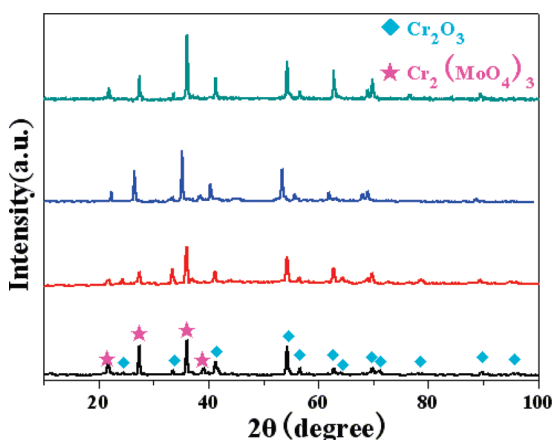**FIGURE 6.** XRD patterns of the nanocrystalline $Mo_5Si_3$ film oxidation test for 5 and 10 min at 800 °C in air.



**FIGURE 7.** XRD patterns of a nanocrystalline $(Mo_{0.57}Cr_{0.43})_5Si_3$ film after oxidation tests for different times at 800 °C in air.

different times of oxidation at 800 °C in air. According to Table 1 and Figure 7, the oxide scales on the surface of nanocrystalline $(Mo_xCr_{1-x})_5Si_3$ ($x = 0.78, 0.75, 0.64, 0.57$) films consist of $Cr_2O_3$, $Cr_2(MoO_4)_3$, and $SiO_2$. No peaks of crystalline $SiO_2$ are observed, confirming that silica formed is amorphous at this oxidation temperature. This is in substantial agreement with the result reported by Ström et al. (28), who found that the oxide products formed on chromium-alloyed $MoSi_2$ after exposure at 450 °C in ambient air for 456 h are $Cr_2(MoO_4)_3$, $MoO_3$, and $SiO_2$.

**Morphologies of Oxide Scales.** After cyclic oxidation at 800 °C for 5 min, a mass of weedlike molybdenum oxide with a Mo/O atomic ratio approaching 3 and local spallation of scale are observed on the nanocrystalline $Mo_5Si_3$ film, as shown in Figure 8. Naked-eye examinations reveal that sample surfaces exhibit white powder after oxidation of 5 min, suggesting that the nanocrystalline $Mo_5Si_3$ film undergoes pesting disintegration. Figure 9 presents the SEM micrograph of the top surface and cross-section of the oxide scale formed on the nanocrystalline $Mo_5Si_3$ film exposed at 800 °C for 10 min. It can be seen that a lot of plate-shaped $MoO_3$ penetrates the silica scale by growing outward from the oxide/$Mo_5Si_3$ film interface, leading to uneven stress distribution of the scale (29). As a volatile oxide, $MoO_3$ has a sublimation temperature of 704 °C and volatilization of $MoO_3$ increases significantly

above750 °C (30, 19, 16). The plate-shaped $MoO_3$ protruded from the scale causing continuous weight losses by volatilization, leaving behind a porous silica on the film surface, where accelerated pesting attack via volume diffusion of $O_2$ readily proceeds (31). Besides, as shown in Figure 9B, the oxide scale is easy to rupture and spall because of internal stresses, resulting from remarkable volume expansion via the formation of a mixed oxidation product, as well as vapor pressure of volatilization of $MoO_3$.

Figures 10−13 show the typical surface morphologies of the oxide scale formed on the nanocrystalline $(Mo_xCr_{1-x})_5Si_3$ ($x = 0.78, 0.75, 0.64, 0.57$) films after oxidation at 800 °C for different times. Obviously, additions of chromium to the $Mo_5Si_3$ film alter its oxidation properties at pest oxidation temperature, and evolution of the oxide-scale morphologies exhibits significant differences with variation of the chromium content. In general, it is observed that oxidation resistance of the nanocrystalline $(Mo_xCr_{1-x})_5Si_3$ films increases with an increase in the chromium content. No pesting behavior is observed for the nanocrystalline $(Mo_xCr_{1-x})_5Si_3$($x = 0.78, 0.75, 0.64, 0.57$) films as compared to the $Mo_5Si_3$ film. Owing to $MoO_3$ evaporated from the surface, the scale on the nanocrystalline $(Mo_{0.78}Cr_{0.22})_5Si_3$ film is porous oxide with a pore size on the order of 6 $\mu$m diameter after 10 h of exposure (Figure 10A). With extension of the exposure time, the surface morphology of unspallation regions becomes rather rough and loose with plenty of cracks (Figure 10B). At the same exposure time (10 h), the pore size for the scale surface on the nanocrystalline $(Mo_{0.75}Cr_{0.25})_5Si_3$ film is reduced to 1 $\mu$m (Figure 11A,B), providing evidence that the mixed oxidation scale is protective, acting as a barrier to the outward diffusion of molybdenum, and has some capability of self-healing by sealing the pores formed at the early stage of oxidation. When the exposure time is extended to 20 h, a mass of spheroid-shaped silicon-rich oxide with cracks is distributed over the scale surface (Figure 11C). This is due to the thermal stresses that originate from the mismatch in the CTE between different phases. A number of cracks and pinholes have been observed on the oxide-scale surface of unspallation regions after 90 h of cyclic oxidation (Figure 11D). Thus, spallation resistance to thermal cycling for the nanocrystalline $(Mo_{0.75}Cr_{0.25})_5Si_3$ film is noticeably enhanced, and the lifetime of scale spallation is an increase of 4.5 times compared with that of the nanocrystalline $(Mo_{0.78}Cr_{0.22})_5Si_3$ film. After an exposure of 10 h, the scale formed on the nanocrystalline $(Mo_{0.64}Cr_{0.36})_5Si_3$ film appears to be flat and dense (Figure 12A), in contrast to the porous scale formed on the two former films. As the exposure time is increased to 90 h, the surface of the oxide scale becomes so smooth that it is difficult to take a clear photo for characterization of the surface morphology by SEM (Figure 12B). The oxide microstructure of the unspallation region still looks fine and uniform after 140 h of cyclic oxidation (Figure 12C). For the nanocrystalline $(Mo_{0.57}Cr_{0.43})_5Si_3$ film, the mixed oxidation scale with dense and fine grains is formed on the whole sample surface after oxidation at 800 °C for different times,
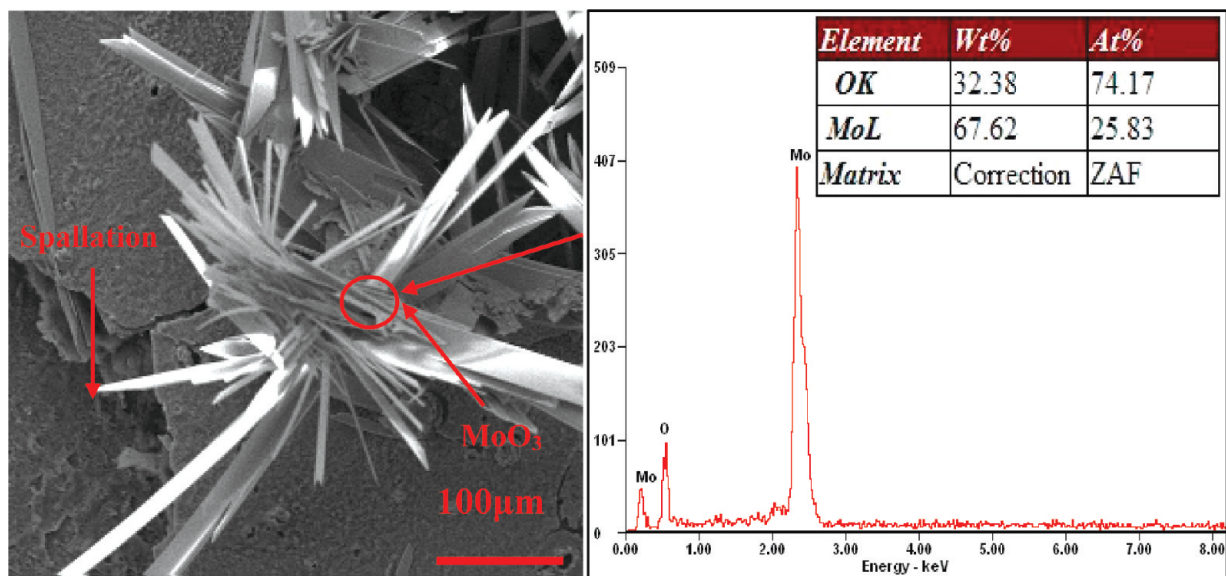
<br>

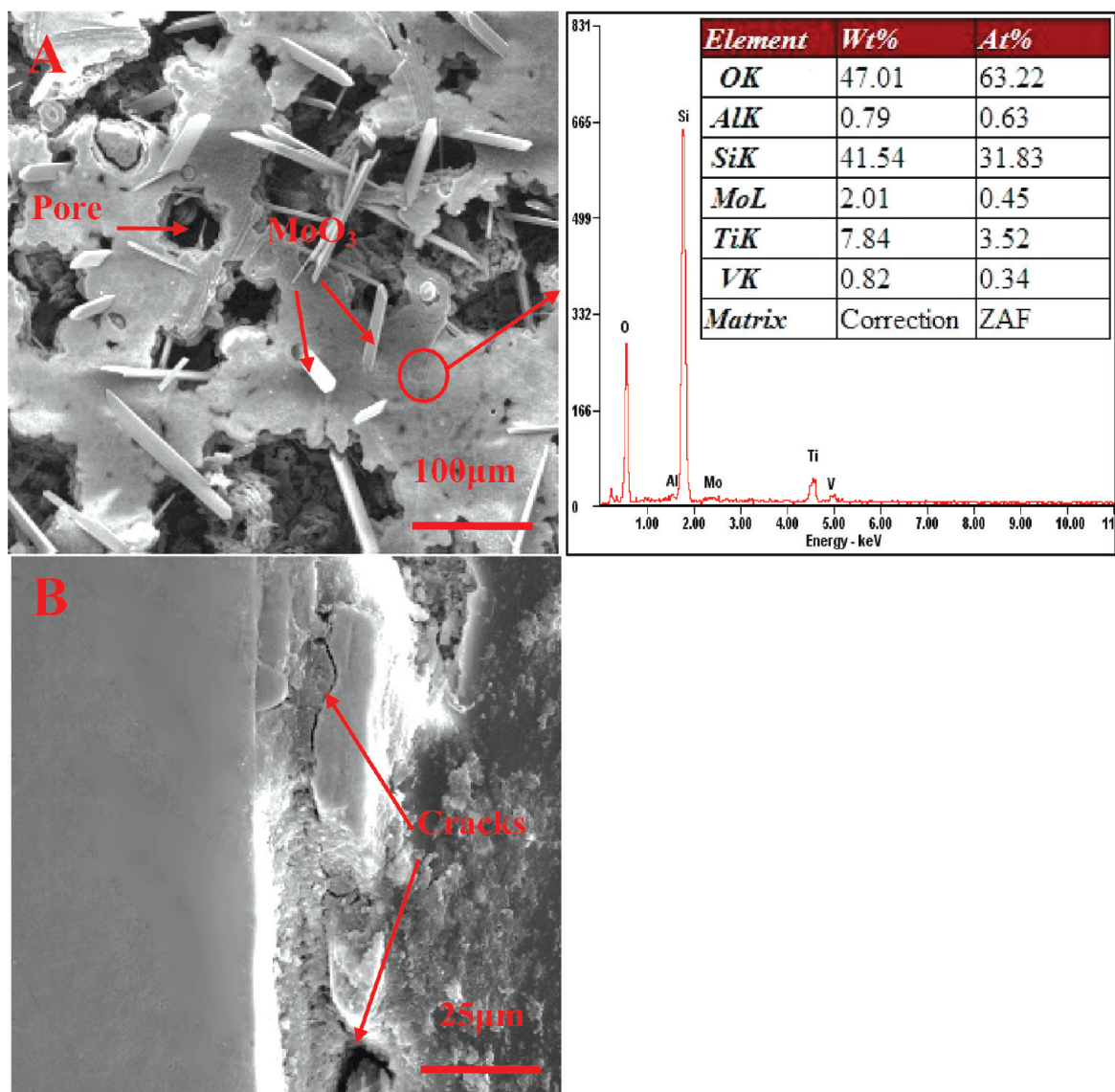FIGURE 8. SEM micrographs of the nanocrystalline Mo$_5$Si$_3$ film oxidized at 800 °C for 5 min.



FIGURE 9. Surface and cross-sectional morphologies of the nanocrystalline Mo$_5$Si$_3$ film oxidized at 800 °C for 10 min.
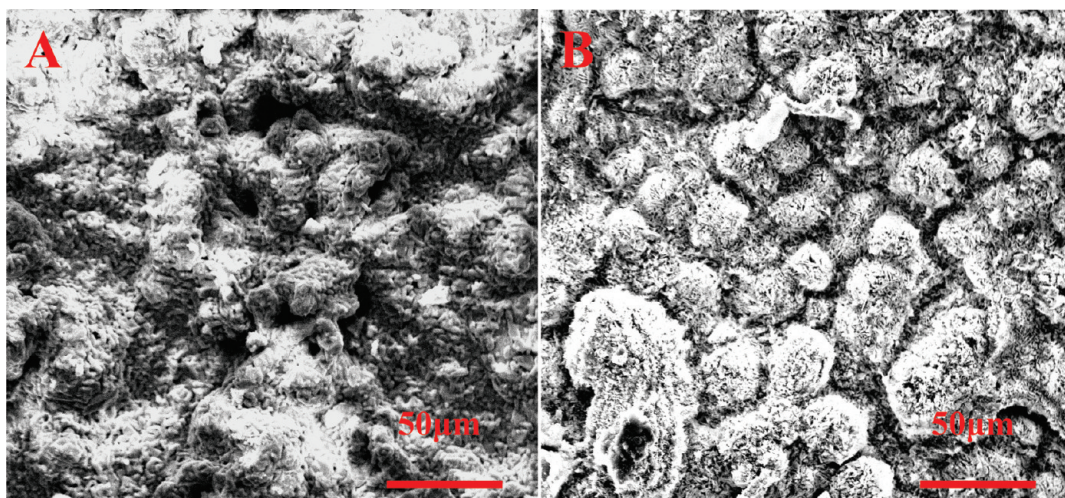
FIGURE 10. SEM micrographs of the top surface of the nanocrystalline $(Mo_{0.78}Cr_{0.22})_5Si_3$ film after oxidation at 800 °C for different times: (A) 10 h; (B) 20 h.
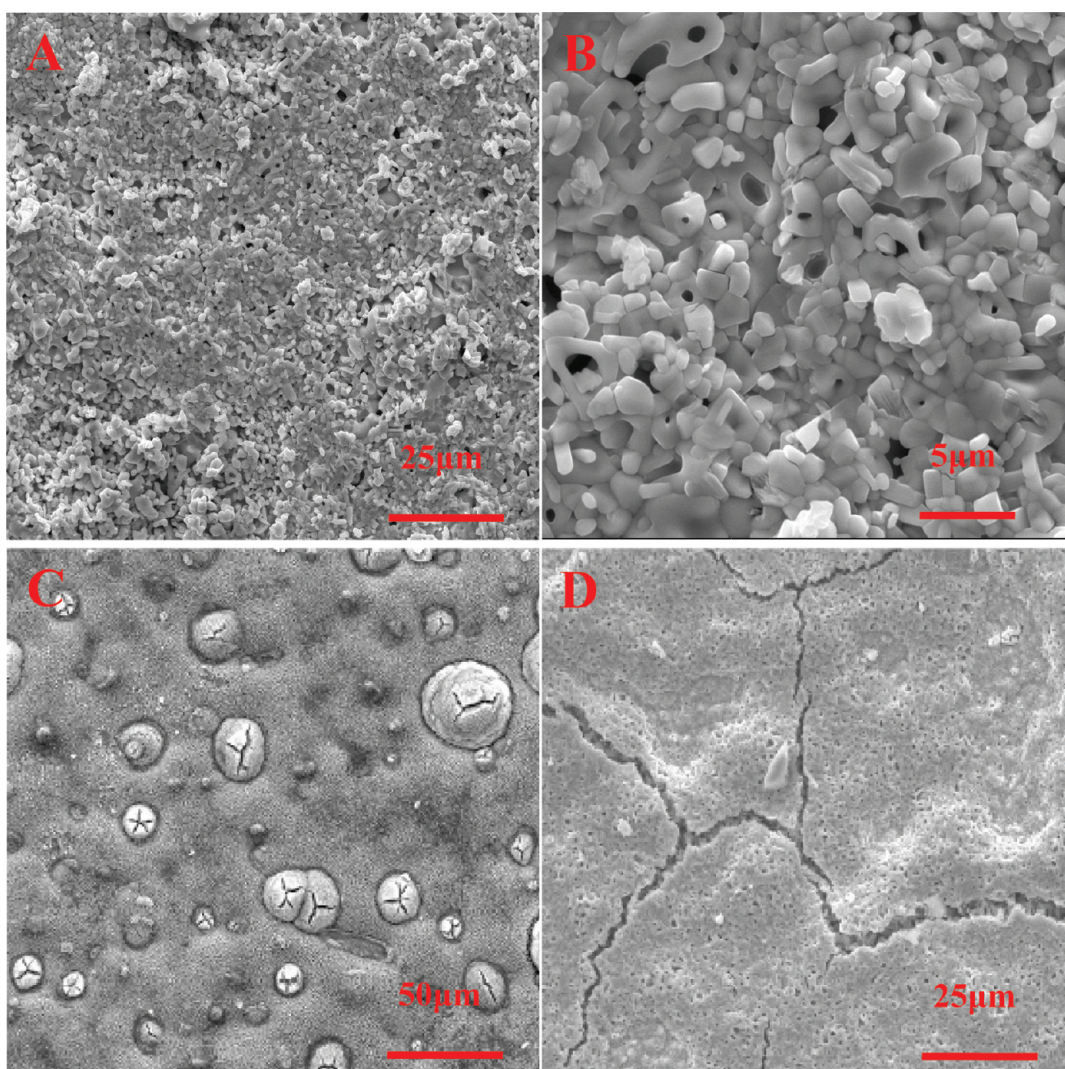


FIGURE 11. SEM micrographs of the top surface of the nanocrystalline $(Mo_{0.75}Cr_{0.25})_5Si_3$ film after oxidation at 800 °C for different times: (A) 10 h; (B) high-magnification micrograph of part A; (C) 20 h; (D) 90 h.
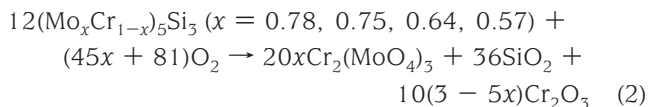
as shown in Figure 13. With an increase in the oxidation test time, the size of the oxide grains is progressively decreased, which is in good agreement with the XRD results (Figure 7), showing that the breadth of the diffraction peaks for oxide

is gradually increased. Figure 14 shows a typical cross-sectional photograph and EDS line profiles of the oxide scale formed on the nanocrystalline $(Mo_{0.57}Cr_{0.43})_5Si_3$ film after oxidation at 800 °C for different times. The oxide scale is

continuous, compact, and tightly adhering to the substrate. EDS line profiles confirm that the amount of $Cr_2(MoO_4)_3$ is relatively rare in the mixed oxide products because of the low content of molybdenum in the scale. Also, it is evident that the thickness changes of the oxide scales are very small with an increase in the oxidation time from 20 to 240 h, indicating that the mixed oxide scale is quite stable.

## DISCUSSION

**Effect of the Chromium Content on the Oxidation Behaviors.** On the basis of XRD analysis and scale morphologies observation, the character of a knee on kinetic curves of nanocrystalline $(Mo_xCr_{1-x})_5Si_3$ ($x = 0.78$, 0.75, 0.64, 0.57) films can be well explained. When the nanocrystalline $(Mo_xCr_{1-x})_5Si_3$ ($x = 1, 0.78, 0.75, 0.64, 0.57$) films are oxidized at 800 °C in air, the following reactions can take place on the surface of the films:

$$2Mo_5Si_3 + 21O_2 \rightarrow 10MoO_3(\text{volatile}) + 6SiO_2 \tag{1}$$

$$12(Mo_xCr_{1-x})_5Si_3 \ (x = 0.78,\ 0.75,\ 0.64,\ 0.57) +$$
$$(45x + 81)O_2 \rightarrow 20xCr_2(MoO_4)_3 + 36SiO_2 +$$
$$10(3 - 5x)Cr_2O_3 \tag{2}$$

Reaction (1) predicts a mass loss during oxidation, which can be mainly attributed to the easy volatilization of molybdenum oxide. On the contrary, reaction (2) predicts a net mass gain due to the formation of nonvolatile oxide products. During an initial period of 10 h, volatile $MoO_3$ is formed by the reaction of Mo atoms at the surface of the specimen with the O atoms in air, leading to the linear mass loss that occurred. Apparently, the magnitude of the initial weight loss is gradually reduced with an increase in the chromium addition. Subsequently, the mass reduction can be definitely suppressed by the formation of protective mixed oxide scales, which played an important role in obstructing or trapping the evaporation of $MoO_3$. Thus, reaction (2) is overwhelming in the competitive mass change process after an exposure of 10 h.

Owing to the strong thermal expansion anisotropy along the $a$ and $c$ directions [CTE($c$)/CTE($a$) = 2.2], significantly



**FIGURE 12. SEM micrographs of the top surface of the nanocrystalline $(Mo_{0.64}Cr_{0.36})_5Si_3$ film after oxidation at 800 °C for different times: (A) 10 h; (B) 90 h; (C) 140 h.**

FIGURE 13. SEM micrographs of the top surface of the nanocrystalline $(Mo_{0.57}Cr_{0.43})_5Si_3$ film after oxidation at 800 °C for different times: (A) 10 h; (B) image magnification of part A; (C) 90 h; (D) 240 h.

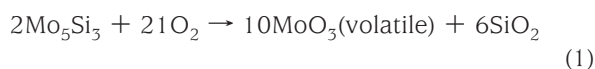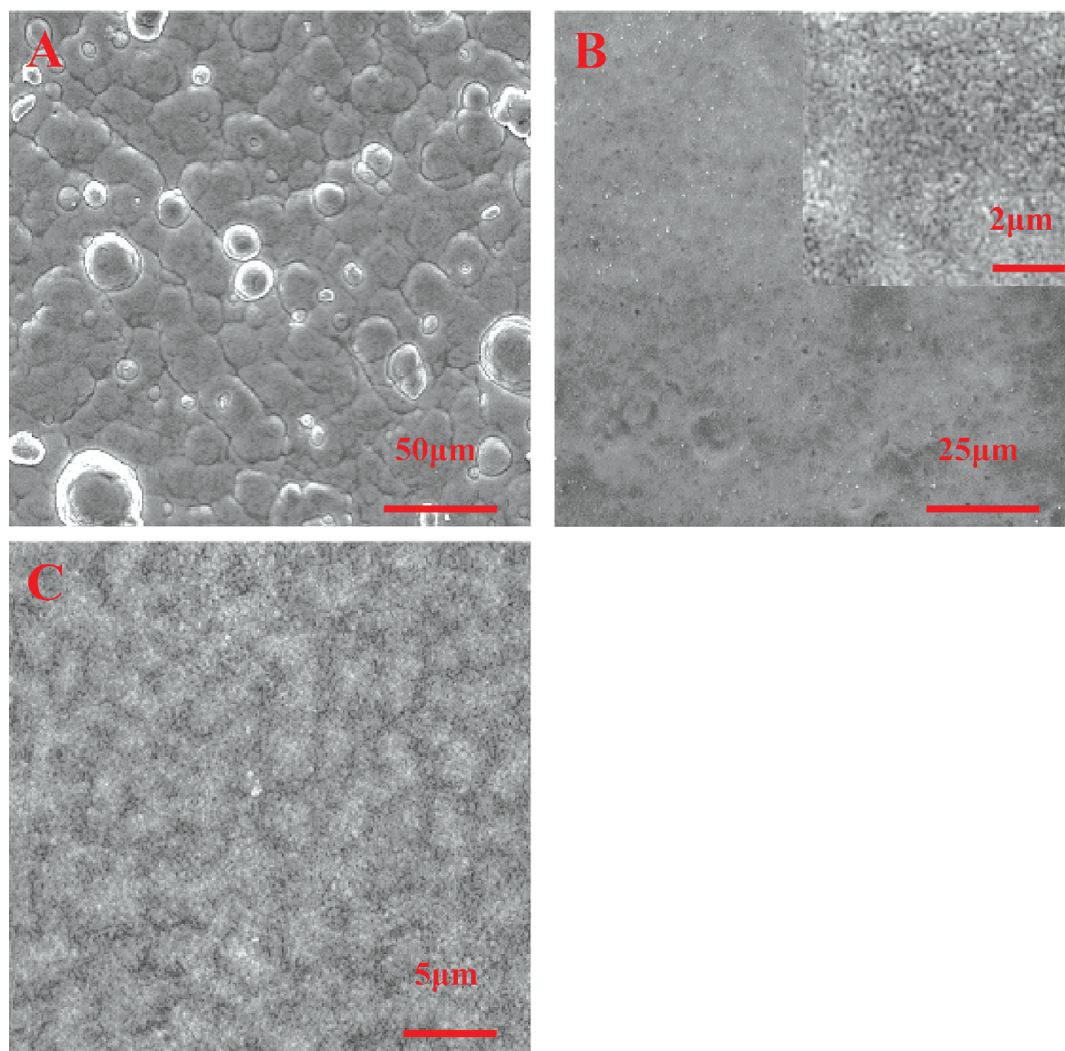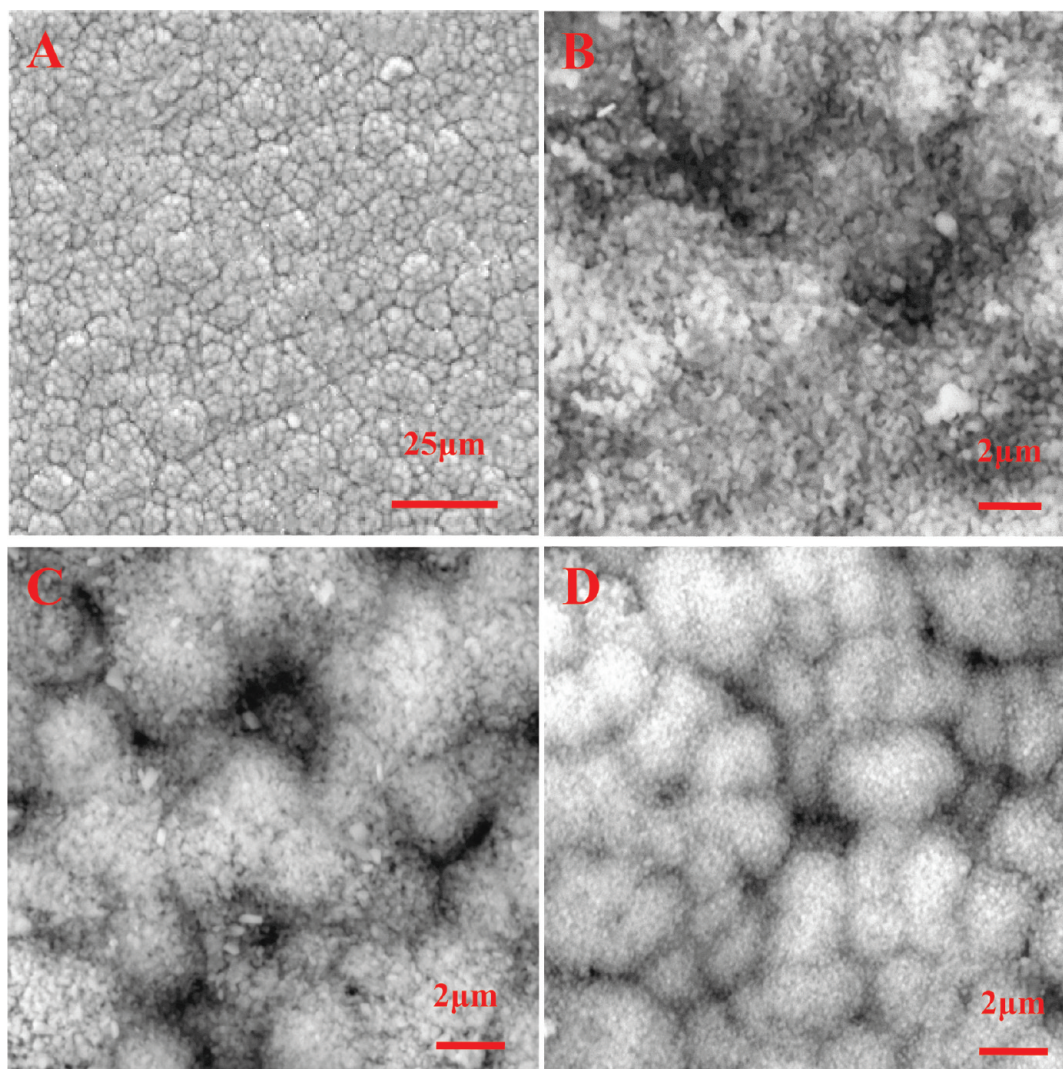large residual thermal stresses can develop in polycrystalline $Mo_5Si_3$ in the solidification process, causing grain boundary cracking (4). Berkowitz-Mattuck et al. (32) attributed the pest oxidation to stress-enhanced oxidation because of the high residual stresses introduced via cooling of anisotropic materials from the melt. This is due to the fact that both $MoO_3$ and silica are formed at the external surface of a crack during the oxidation process, which forms a wedging effect (33). Chromium additions increase the CTE in both the *a* and *c* directions, and the CTE-mismatch decreases with an increase in the addition of chromium to $Mo_5Si_3$. As the chromium content is increased to 25 atom %, the CTE(*c*)/CTE(*a*) ratio is reduced from 2.0 to 1.55 (34, 5). On the basis of metallographic observations (Figures 3 and 14), the nanocrystalline $(Mo_xCr_{1-x})_5Si_3$ films are free of microcracks under conditions of as-deposited or after a certain number of cyclic oxidations, which suggests that the thermal stresses should have been relieved and thus the spallation resistance of the films are improved.

**Effect of Nanocrystalline Films on the Oxidation Behaviors.** It is generally accepted that the nanostructure has shown a positive effect for the enhance-

ment of the oxidation resistance of materials. Wang et al. (35, 36) have reported that the sputtered nickel-based nanocoatings (grain size below 100 nm) possessed much better oxidation resistance than as-cast alloys with the same chemical composition. In our work, there are two aspects of the effects of nanocrystalline films on the oxidation behaviors of $(Mo_xCr_{1-x})_5Si_3$ ($x = 1$, 0.78, 0.75, 0.64, 0.57) films, including the positive aspect and its negative effect. Nanocrystalline materials have a high density of grain boundaries, which act as short-circuit diffusion paths for oxygen transport to the oxidation interface and outward diffusion of the alloy element during oxidation (37). For the nanocrystalline $Mo_5Si_3$ film, grain boundaries, as high-energy sites, are preferentially oxidized, accelerating the outward growth of $MoO_3$, as shown in Figure 9A. This induces a nonuniform growth and expansion within the oxide scale, accompanied by uneven stress distribution of the scale. When the accumulated stress has eventually come to surpass the compression strength of the scale, cracks are easily initiated and propagate, leading to the quick occurrence of pest disintegration. Therefore, a nanocrystalline film has an adverse effect on the oxidation resistance of $Mo_5Si_3$.
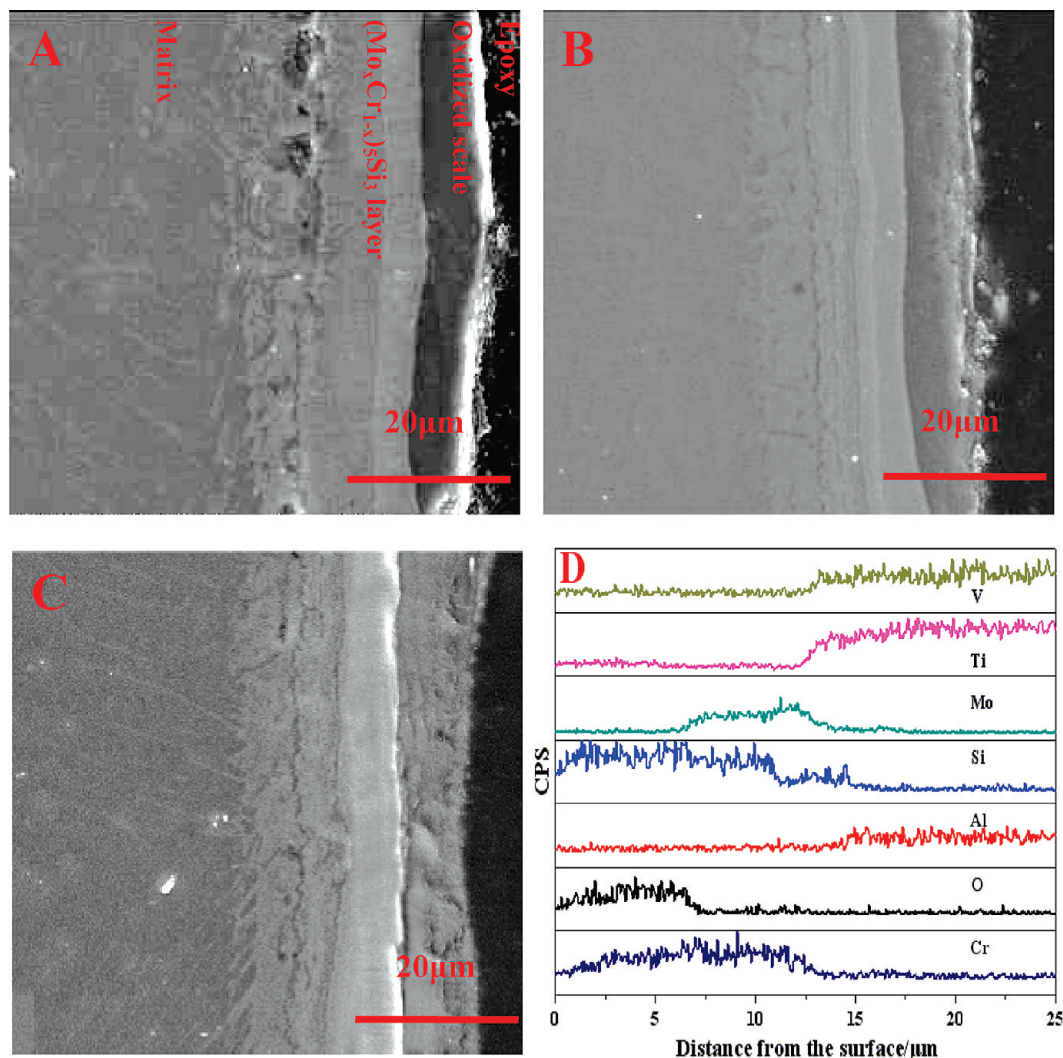
**FIGURE 14. Micrographs of scale cross-sectional morphologies of the nanocrystalline $(Mo_{0.57}Cr_{0.43})_5Si_3$ film after oxidation at 800 °C for different times: (A) 20 h; (B) 90 h; (C) 240 h; (D) element line scanning EDS analyses of the $(Mo_{0.57}Cr_{0.43})_5Si_3$ film after oxidation at 800 °C for 240 h.**

On the contrary, a nanocrystalline film plays a useful role in improving the oxidation behaviors of $(Mo_xCr_{1-x})_5Si_3$ ($x =$ 0.78, 0.75, 0.64, 0.57) films. Chromium, as a protective scale-forming element, can participate in the formation of an oxide scale, resulting in the structural and compositional changes of the oxide scale. The abundant density of grain boundaries is preferred nucleation sites for forming oxides, inferring that internuclei spacing is much closer and the time needed for the linking of the neighboring oxide nuclei to form a continuous layer is shortened (38, 39). When the protective and stable oxide scale is formed, the formation of a highly volatile molybdenum oxide is suppressed because of the fact that migration of molybdenum from the underlying films toward the surface is effectively prevented. As shown in Figures 12 and 13, the grain size of the mixed oxide scale formed on the nanocrystalline $(Mo_xCr_{1-x})_5Si_3$ films after oxidation at 800 °C for different times is only 100−200 nm. The similar results reported by Liu et al. (40) showed that the average grain size of an $Al_2O_3$ scale formed on nickel-based nanocoatings (grain size about 65 nm) is below 200 nm. The oxidation scales with fine grains are favorable to relieve the thermally induced stress by diffusion creep of the oxide scale. The following equation is used as the basis for estimating the creep rate of the oxide scale or the base metal at high temperatures (41):

$$\varepsilon = \frac{\sigma\Omega}{d^2 kT}\left(B_1 D_V + \frac{B_2 \delta D_B}{d}\right) \tag{3}$$

where $\sigma$ is the applied tensile stress, $\Omega$ is the atomic volume, $d$ is the average grain size, $B_1$ and $B_2$ are constants, $D_V$ and $D_B$ are the diffusion coefficients along the grain boundaries and through the lattice, $\delta$ is the width of the grain boundaries, and $k$ is Boltzmann's constant. Equation 3 indicates that the smaller the grain size of the alloy and oxide, the greater the creep rates. Therefore, the spallation tendency of scale is reduced through diffusion creep, and adhesion between the oxide scales and the nanocrystalline $(Mo_xCr_{1-x})_5Si_3$ ($x =$ 0.78, 0.75, 0.64, 0.57) films is effectively improved.

## CONCLUSIONS

In summary, five kinds of sputter-deposited nanocrystalline $(Mo_xCr_{1-x})_5Si_3$ ($x =$ 1, 0.78, 0.75, 0.64, 0.57) films have

been successfully prepared on Ti−6A1−4 V alloy substrates by double-cathode glow discharge. The microstructural analysis of the sputter-deposited films indicates that the films are composed of an outer $(Mo_xCr_{1-x})_5Si_3$ layer with an average grain size of 8 nm and an inner diffusion layer. The unalloyed $Mo_5Si_3$ film shows a pest reaction immediately after a few minutes of oxidation in air. On the contrary, spallation resistance to thermal cycling for nanocrystalline chromium-alloyed $Mo_5Si_3$ films is significantly improved with an increase in the chromium addition, and particularly for $(Mo_{0.57}Cr_{0.43})_5Si_3$ film, no sign of spallation or microcracking occurred after exposure at 800 °C in ambient air for 240 h because of the formation of a fine-grain protective scale. A coupling effect of the nanosize crystal and substitution of chromium for molybdenum are beneficial to improving the oxidation behaviors of nanocrystalline $(Mo_xCr_{1-x})_5Si_3$ ($x$ = 0.78, 0.75, 0.64, 0.57) films.

## REFERENCES AND NOTES

(1) Yeh, C. L.; Chen, W. H. *J. Alloys Compd.* **2007**, *439*, 59–66.
(2) Yeh, C. L.; Wang, H. J. *Intermetallics* **2007**, *15*, 1277–1284.
(3) Chen, Z.; Yan, Y. W. *J. Alloys Compd.* **2006**, *413*, 73–76.
(4) Chu, F.; Thoma, D. J.; McClellan, K. J.; Peralta, P. *Mater. Sci. Eng., A* **1999**, *261*, 44–52.
(5) Ström, E.; Eriksson, S.; Rundlöf, H.; Zhang, J. *Acta Mater.* **2005**, *53*, 357–365.
(6) Ström, E. *Mater. Charact.* **2005**, *55*, 402–411.
(7) Mason, D. P.; Van Aken, D. C. *Acta Metall. Mater.* **1995**, *43*, 1201–1210.
(8) Yoshimi, K.; Yoo, M. H.; Wereszczak, A. A.; Borowicz, S. M.; George, E. P.; Miura, E.; Hanada, S. *Mater. Sci. Eng., A* **2002**, *329−331*, 228–234.
(9) Shaked, H.; Jorgensen, J. D.; Short, S.; Chmaissem, O.; Ikeda, S. I.; Maeno, Y. *Phys. Rev. B* **2000**, *62*, 8725–8730.
(10) Lizuka, T.; Kita, H. *Mater. Sci. Eng., A* **2004**, *366*, 10–16.
(11) Ingemarsson, L.; Halvarsson, M.; Hellström, K.; Jonsson, T.; Sundberg, M.; Johansson, L.-G.; Svensson, J.-E. *Intermetallics* **2010**, *18*, 77–86.
(12) Natesan, K.; Deevi, S. C. *Intermetallics* **2000**, *8*, 1147–1158.
(13) Liu, Y. Q.; Shao, G.; Tsakiropoulos, P. *Intermetallics* **2001**, *9*, 125–136.
(14) Meyer, M. K.; Akinc, M. *J. Am. Ceram. Soc.* **1996**, *79*, 938–944.
(15) Rosales, I.; Martinez, H.; Bahena, D.; Ruiz, J. A.; Guardian, R.; Colin, J. *Corros. Sci.* **2009**, *51*, 534–538.
(16) Akinc, M.; Meyer, M. K.; Kramer, M. J.; Thom, A. J.; Huebsch, J. J.; Cook, B. *Mater. Sci. Eng., A* **1999**, *261*, 16–23.
(17) Petrovic, J. J.; Vasudevan, A. K. *Mater. Sci. Eng., A* **1999**, *261*, 1–5.
(18) Feng, P. Z.; Wang, X. H.; He, Y. Q.; Qiang, Y. H. *J. Alloys Compd.* **2009**, *473*, 185–189.
(19) Ochiai, S. *Intermetallics* **2006**, *14*, 1351–1357.
(20) Ochiai, S. *Mater. Sci. Forum* **2003**, *426−432*, 1771–1776.
(21) Xu, J.; Xu, Z.; Tao, J.; Liu, Z. L.; Chen, Z. Y.; Zhu, W. H. *Scr. Mater.* **2007**, *57*, 587–590.
(22) Xu, J.; Sun, J.; Jiang, S. Y. *Mater. Lett.* **2009**, *63*, 1082–1084.
(23) Rahman, A.; Jayaganthan, R.; Prakash, S.; Chawla, V.; Chandra, R. *J. Alloys Compd.* **2009**, *472*, 478–483.
(24) Çelik, A.; Bayrak, Ö.; Alsaran, A.; Kaymaz, İ.; Yetim, A. F. *Surf. Coat. Technol.* **2008**, *202*, 2433–2438.
(25) Ström, E.; Zhang, J.; Eriksson, S.; Li, C. H.; Feng, D. *Mater. Sci. Eng., A* **2002**, *329−331*, 289–294.
(26) Cox, A. R.; Brown, R. *J. Less-Common Met.* **1964**, *6*, 51.
(27) Peng, X. M.; Xia, C. Q.; Liu, Y. Y.; Wang, J. H. *Surf. Coat. Technol.* **2009**, *203*, 3306–3311.
(28) Ström, E.; Cao, Y.; Yao, Y. M. *Trans. Nonferrous Met. Soc. China* **2007**, *17*, 1282–1286.
(29) Stergiou, A.; Tsakiropoulos, P. *Intermetallics* **1997**, *5*, 117–126.
(30) Paswan, S.; Mitra, R.; Roy, S. K. *Intermetallics* **2007**, *15*, 1217–1227.
(31) Chou, T. C.; Nieh, T. G. *JOM* **1993**, *45*, 15–21.
(32) Berkowitz-Mattuck, J. B.; Rosetti, M.; Lee, D. W. *Metall. Trans.* **1970**, *1*, 479–483.
(33) Yanagihara, K.; Przybylski, K.; Maruyama, T. *Oxid. Met.* **1997**, *47*, 277–293.
(34) Schneibel, J. H.; Rawn, C. J.; Payzant, E. A.; Fu, C. L. *Intermetallics* **2004**, *12*, 845–850.
(35) Wang, F.; Tian, X.; Li, Q.; Li, L.; Peng, X. *Thin Solid Films* **2008**, *516*, 5740–5747.
(36) Lou, H.; Tang, Y.; Sun, X.; Guan, H. *Mater. Sci. Eng., A* **1996**, *207*, 121–128.
(37) Liu, Z.; Gao, W.; Dahm, K.; Wang, F. *Acta Mater.* **1998**, *46*, 1691–1700.
(38) Cao, G. J.; Geng, L.; Zheng, Z. Z.; Naka, M. *Intermetallics* **2007**, *15*, 1672–1677.
(39) Perez, P. *Corros. Sci.* **2002**, *44*, 1793–1808.
(40) Liu, Z. Y.; Gao, W.; Dahm, K.; Wang, F. H. *Scr. Mater.* **1997**, *37*, 1551–1558.
(41) Liu, Z.; Gao, Y. W.; Wang, F. H. *Scr. Mater.* **1998**, *39*, 1497–1502.

AM900794F